Title

Data-efficient resting-state functional magnetic resonance imaging brain mapping with deep learning.

Journal

Journal of Neurosurgery, 139(5)

Authors

Luckett, Patrick

Park, Ki

Lee, John

et al.

Publication Date

2023-11-01

DOI

10.3171/2023.3.JNS2314

Peer reviewed

HHS Public Access

Author manuscript

J Neurosurg. Author manuscript; available in PMC 2024 May 01.

Published in final edited form as:

J Neurosurg. 2023 November 01; 139(5): 1258–1269. doi:10.3171/2023.3.JNS2314.

Data Efficient Resting State Functional MRI Brain Mapping with Deep Learning

Patrick H. Luckett, PhD[1], **Ki Yun Park, BS**[1,8], **John J. Lee, MD, PhD**[2], **Eric J Lenze, MD**[4], **Julie L Wetherell, PhD**[5,6], **Lisa Eyler, PhD**[6], **Abraham Z. Snyder, MD, PhD**[2,7], **Beau M. Ances, MD, PhD, MSc**[7], **Joshua S. Shimony, MD, PhD**[2], **Eric C. Leuthardt, MD**[1,8,9,10,11,12,13]

[1]Division of Neurotechnology, Department of Neurological Surgery, Washington University School of Medicine, St. Louis, Missouri

[2]Mallinckrodt Institute of Radiology, Washington University School of Medicine, St. Louis, Missouri

[4]Department of Psychiatry, Washington University School of Medicine, St. Louis, Missouri

[5]Mental Health Impact Unit 3, VA San Diego Healthcare System, San Diego, California

[6]Department of Psychiatry, University of California, San Diego, California

[7]Department of Neurology, Washington University School of Medicine, St. Louis, Missouri

[8]Department of Neuroscience, Washington University School of Medicine, St. Louis, Missouri

[9]Department of Biomedical Engineering, Washington University in St. Louis, St. Louis, MO

[10]Department of Mechanical Engineering and Materials Science, Washington University in St. Louis, St. Louis, MO

[11]Center for Innovation in Neuroscience and Technology, Division of Neurotechnology, Washington University School of Medicine, St. Louis, MO

[12]Brain Laser Center, Washington University School of Medicine, St. Louis, Missouri

[13]National Center for Adaptive Neurotechnologies

Abstract

Objective: Resting state functional MRI (RS-fMRI) enables mapping of function within the brain, and is emerging as an efficient tool for pre-surgical evaluation of eloquent cortex. Models capable of reliable and precise mapping of resting state networks (RSN) with reduced scanning time would lead to improved patient comfort while reducing cost per scan. The aims of this study were to develop a deep 3D convolutional neural network (3DCNN) capable of voxelwise mapping of language (LAN) and motor (MOT) resting state networks (RSN) with minimal quantities of RS-fMRI data.

Methods: Imaging data was gathered from multiple ongoing studies at Washington University School of Medicine and other thoroughly characterized, publicly available data sets. All study participants (n=2252 healthy adults) were cognitively screened and completed structural

Corresponding author: Patrick H. Luckett, PhD, Department of Neurological Surgery, Washington University School of Medicine, 660 S. Euclid Avenue, Campus Box 8057, St. Louis, MO 63110, luckett.patrick@wustl.edu.

neuroimaging and RS-fMRI. Random permutations of RS-fMRI regions of interest were used to train a 3DCNN. After training, model inferences were compared using varying amounts of RS-fMRI data from the control data as well as five patients with glioblastoma multiforme.

Results: The trained model achieved 96% out of sample validation accuracy on data encompassing a large age range collected on multiple scanner types and varying sequence parameters. Testing on out of sample control data showed 97.9% similarity between results generated using either 50 or 200 RS-fMRI time points, corresponding to approximately 2.5 and 10 minutes respectively (96.9% LAN, 96.3% MOT true positive rate). In evaluating data from patients with brain tumors, the 3DCNN was able to accurately map LAN and MOT networks in spite of structural and functional alterations.

Conclusion: Functional maps produced by the 3DCNN can inform surgical planning in patients with brain tumors in a time-efficient manner. We present a highly efficient method for pre-surgical functional mapping, hence, improved functional preservation in patients with brain tumors.

Keywords

Deep learning; resting state functional MRI; brain tumor

1. Introduction

MRI-based brain imaging is an integral part of patient care and medical research. Biomarkers of the neuropathogenesis and neurological manifestation of brain disorders can be identified by structural and/or functional MRI[1]. Most notably, MRI is of crucial importance for preoperative and intraoperative localization in brain tumor patients. Optimization of patient outcomes requires a balance between maximal extent of resection, which can reduce symptoms and extend the time until tumor recurrence, versus functional preservation, which impacts post-surgical quality of life. Structural MRI is routinely used by surgeons to identify the location and extent of resection necessary for maximal long-term survival. Functional MRI has been employed for preoperative planning, with the goal of minimizing the risk of functional impairment[2,3]. Studies have shown that gross total resection (as opposed to subtotal resection) in patients with gliomas leads to extended length of survival[4]. However, greater extent of resection increases the likelihood of functional deficits[5]. Specifically, deficits in language and motor networks have been shown to significantly impact quality of life[4].

Functional MRI (fMRI) has emerged as a powerful tool for mapping clinically relevant functional brain areas (“eloquent cortex”) using the blood oxygen level dependent (BOLD) signal[6,7]. In current clinical practice, task-fMRI (T-fMRI) is most often used to “activate” particular parts of the brain (e.g., finger tapping to activate the hand motor area)[8]. However, recent work has demonstrated that these same regions can be mapped by appropriate analysis of task-free fMRI (“resting state” fMRI, RS-fMRI)[9,10]. Functionally related constellations of brain regions are widely known as resting state networks (RSNs)[11]. Multiple RSNs have been associated with specific sensory, motor and cognitive functions[12,13]. A major advantage of RS-fMRI is that RSNs can be mapped without the need for patient compliance with a task paradigm. Further, RS-fMRI can be acquired even under

sedation. Moreover, the failure rate of RS-fMRI is lower than that of task-based fMRI[14]. Thus, RS-fMRI may be optimal as a means of mapping the representation of function in the clinical setting.

A primary issue concerning RS-fMRI is the length of acquisition time required to obtain reliable data. The precision of RSN mapping using conventional computational techniques (Pearson correlation) fundamentally depends on the quantity of acquired data[15]. Acquisition time is important for multiple reasons. First, the likelihood that a patient will have significant head motion and/or fall asleep in the scanner, both of which can lead to systemic alterations in structural and functional MRI results, increases with longer scan times[16,17]. Further confounding the issue is the fact that, in general, multiple sequences (e.g., T1 pre- and post-contrast, T2, DTI, fMRI, SWI, ASL) are collected during a single scan session. In these circumstances, scanner time must be optimized in a manner that allows for reliable imaging data while still minimizing the total time in the scanner. Thus, computational models capable of reliable image reconstruction with less data could lead to less scan time, increased efficiency, and lower cost.

Convolutional Neural Networks (CNN) are a type of deep learning model inspired by the visual system. Applications of CNNs range from object detection and classification to natural language processing[18]. Pertaining to structural MRI, multiple studies have demonstrated the ability of CNNs to meet the state of the art in tumor segmentation, image inverse problems (recovering/reconstructing images from sets of noisy measurements), reducing the amount of contrast necessary for MRI scans, and reducing the sequence time necessary to obtain high resolution images[19–21]. To a lesser extent, CNNs have also been applied to functional MRI, predominantly for disease classification[22,23].

This study utilizes a large cohort of healthy participants (n=2252) to develop a 3D convolutional neural network (3DCNN) capable of efficient and accurate voxelwise mapping of language and motor RSNs with less than 5 minutes of data. After training, model results were compared using varying amounts of RS-fMRI data from a thoroughly characterized publically available fMRI data set[24]. Further, we compare functional maps generated with the 3DCNN to aggregated task fMRI (T-fMRI) maps compiled in the Neurosynth platform (www.neurosynth.org)[25]. Lastly, model results were evaluated on five patients retrospectively recruited from the Neurosurgery brain tumor service at Washington University School of Medicine[26]. Our results indicate that the 3DCNN is capable of reliable functional mapping with minimal amounts of data in both healthy controls and patients with brain tumors. Further, stable results were achieved on data encompasing a wide age range, multiple scanner types, and multiple scanner sequences. This technology has the potential to improve patient outcomes and reduce costs in patients requiring functional imaging.

2. Methods

2.1 Participants

Normal human RS-fMRI data (n=2252) were obtained from publicly available data sets[27,28] and internal studies at Washington University in St. Louis (Table 1). All participants were cognitively normal based on study-specific performance testing. The appropriate

Institutional Review Board approved all studies, and all participants provided written informed consent for the use of their de-identified data.

2.2 Magnetic resonance imaging (MRI) acquisition

All imaging was performed on 3T Siemens scanners (Siemens AG, Erlangen, Germany) equipped with the standard 12-channel head coil. A high-resolution, 3-dimensional, sagittal, T1-weighted, magnetization-prepared rapid gradient echo scan (MPRAGE) was acquired (echo time [TE] = 1.54–16 ms, repetition time [TR] = 2200–2,400 ms, inversion time = 1,000–1100 ms, flip angle = 7–8°, 256 × 256 acquisition matrix, 1.0–1.2 mm^3 voxels). RS-fMRI scans were collected using an echo planar sequence (voxel size = 3–4 mm^3, TR = 2200–3000 ms, FA = 80°-90°) sensitive to BOLD contrast. Resting state fMRI data was processed using standard methods developed at Washington University[29]. Multi-echo data was collected on either a Siemens scanner equipped with a 20-channel head coil or a GE MR750 3T MRI scanner (GE, Milwaukee, WI) equipped with an eight channel head coil. Structural imaging included T1-weighted (MP-RAGE; TR = 2,400 ms, TE = 3.036–3.16 ms, TI = 1,000 ms; 1 × 1 × 1 mm voxels) and T2-weighted (TR = 2,500–3,200 ms, TE = 73.37–458 ms; 1 × 1 × 1 mm voxels) anatomical images. RS-fMRI was acquired with a multi-echo sequence (TR = 2740–2,960 ms, TE = 14.8–15, 28.4–31.3, 42–47.6, 55.6–63.9 ms; 4 × 4 × 4 mm voxels)[30].

2.3 MRI processing

RS-fMRI data were preprocessed using previously described techniques[31]. Preprocessing included compensation for slice dependent time shifts, elimination of systemic odd-even slice intensity differences (for interleaved, single-echo data), and rigid body correction for head movement. Atlas transformation was achieved by composition of affine transforms connecting the fMRI volumes with the T2-weighted and MPRAGE structural images, resulting in a volumetric time series registered to the MNI152 template in (3 mm cubic) atlas space. In tumor patients, due to the compromised quality of atlas registration owing to destruction of normal tissue and anatomical distortions, non-linear registration with cost-function masking was used as described in[32]. In brief, the warping map was computed using the Advanced Normalization Tools (ANTs) diffeomorphic algorithm registration (https://www.nitrc.org/projects/ants) with a tumor mask. The affine transformation matrix and deformation fields were composed to register structural images to the MNI152 nonlinear asymmetric atlas as the standard template (http://nist.mni.mcgill.ca/?p=904). Additional preprocessing included spatial smoothing (6 mm full width half maximum Gaussian blur in 3D), voxelwise removal of linear trends over each run, and temporal low pass filtering retaining frequencies <0.1 Hz. Spurious variance was reduced by regression of nuisance waveforms derived from head motion correction and extraction of the time series from regions of white matter and CSF segmented by FreeSurfer[33]. The global signal was included as a nuisance regressor[34]. Frame censoring was performed to minimize the impact of head motion[29,35]. All RS-fMRI data were resampled in standard atlas space. Similar methods were used for the multi-echo data after weighted averaging of the echos[30].

2.4 3DCNN

A 3D convolutional neural network (3DCNN) with 60 layers was trained to classify each voxel as belonging to the motor (MOT), language (LAN), or other (OTH) RSN. The 3DCNN had a densely connected architecture[36] that included residual layers nested within dense blocks. One, three, and seven cubic convolutions were performed. Each dense block was directly connected to the cross entropy layer after global average pooling and 20% dropout. Layers were generally arranged as convolution→ batch normalization→ "Swish" activation. Max pooling (2x2x2 with stride 2) was used between dense blocks for dimensionality reduction. Training was terminated if the accuracy did not improve after 3 validations. The 3DCNN was implemented in Matlab R2021b (www.mathworks.com).

2.5 Training Data

Training data was generated by random subsampling of voxels previously shown to belong to either the MOT, LAN, or OTH RSN, where OTH is defined as not MOT or LAN[37]. Subsamples of voxels in a given network were averaged and used to classify the signal into one of the three RSNs based on the highest correlation between the mean subsampled signal and the mean signal for each network. Then, a 3D similarity map was generated by computing the distance correlation between the mean of the subsampled BOLD signals and every other voxel in the brain. Only 50–75 time points from the original BOLD signal were used to generate the 3D similarity map, thereby simulating a short scan duration. However, all time points were used to label the sample into one of the three classes. The exact number of subsampled voxels and the number of time points used for each voxel was generated by a uniform random number generator. This process was repeated multiple times for each network and for each data sample. A total of 1,501,970 training instances were generated across all networks. The number of per-network training samples was approximately equal to ensure the model did not favor a particular class. During training, samples were augmneted by a combination of 3D random affine transformations (rotations (±15 mm), translations (±15 mm)), scaling (between 0.9–1.1), sheering (±15 mm), and adding gaussian noise. Two hundred BOLD scans from our training data set were reserved as validation data for the 3DCNN. Approximately 200,000 validation samples were generated from the held out scans. Training and validation samples were stratified by age, sex, and study. Once the model was fully trained and validated, the 3D similarity maps generated for testing were constructed in the same manner as above. However, each map was derived from a single voxel's time series (as opposed to the mean of random subsamples).

2.6 Testing Data

After training, model outputs were compared using data from the midnight scan club[24] (MSC). The MSC contains data collected on 10 participants each with 10 scanning sessions with 30 minutes of RS-fMRI per session. MSC data was used to compare model results when using different sequence lengths (~2.5 vs ~10 minutes). Further, the trained classifier was tested on data acquired in 5 patients retrospectively recruited from the Neurosurgery brain tumor service at Washington University School of Medicine. Similarity between results was measured using accuracy, boundary F1, DICE, and multiscale structural similarity index (MSSI). Lastly, model results were compared with task activation maps

derived from the Neurosynth platform (neurosynth.org), which generates statistical maps of significance of T-fMRI responses to behavioral paradigms[25]. Neurosynth compiles and aggregates information from published T-fMRI studies, and extracts brain regions that are consistently reported in the literature based on pre-defined terms associated with task responses. The terms used in our analysis were “language” and “motor”. Similarity between 3DCNN and T-fMRI results were measured using MSSI.

2.7 Data and Code Availability

The data used in this study are partially available by request through the appropriate online repositiory[27,28]. Other data may be made available after approval from the appropriate study PIs. Code will be made available upon request.

3. Results

Demographics of the cohort

Participant demographics are shown in Table 1. A majority of the cohort were Caucasian (71%) and female (60%), with an average age of 46.6±23.1 years (range 18–89 years) and 15.1±2.4 years of education.

3.1 Model Results—The model achieved 96% out of sample validation accuracy (Supplemental Figure 1). After training, the MSC data was processed with the 3DCNN first using 10 minutes of available data (MSC200), then using only 2.5 minutes of data (MSC50). Figures 1 and 2 show the results for LAN and MOT, respectively. Highly symmetric results are characteristic of RS-fMRI analysis. Only minor differences were observed between the results from MSC200 and MSC50. Figure 3 and Supplemental Table 1 provides the similarity measures that accompany Figures 1 and 2. Figure 3 left shows the confusion matrix when comparing the winner take all (WTA) voxelwise results for the MSC200 vs MSC50 results. The overall accuracy when treating MSC200 as the “true class” and MSC50 as the “predicted class” was 97.9%. The true positive rate (TPR) for all networks was greater than 96%, as well as the positive predictive value (PPV) for MOT and OTH. The lowest similarity measure observed was PPV for LAN, which was 85.7%. Figure 3 right shows the difference in softmax probabilities (MSC200-MSC50) produced by the 3DCNN for all networks. The majority of voxelwise probability differences were between [-.1, .1]. Further support for the high similarity between the two analyses can be seen in Supplemental Table 1, with the Boundary F1, MSSI, and Dice score showing high values for all networks, as well as low STD between the scores computed across the individual MSC subjects. Similar to Figure 3, the lowest scores were observed in LAN.

Figure 4 shows the comparison of the 3DCNN probability maps averaged over the MSC data, with T-fMRI maps generated from the Neurosynth platform. When calculating the 3DCNN probability maps, only 2.5 minutes of data were used. Of note, the LAN results from RS-fMRI analysis are more symmetric than that seen with T-fMRI. A high degree of similarity was observed for both networks, with an MSSI of 0.83 for LAN and 0.80 for MOT. In total, MOT maps generated from Neurosynth covered 26.2% of the total area of the gray matter, while the 3DCNN maps derived from RS-fMRI only covered 12.5% (0.2

threshold). Similairly, Neurosynth LAN covered 12.9% of the total area and the 3DCNN 9.3%.

To assess the ability of the 3DCNN to accurately map functional networks in the presence of pathological structural and functional alterations, we analyzed retrospective data from 5 patients with glioblastoma multiforme. Figure 5 and 6 shows these results. Again, for these analysis, only 2.5 minutes of data were used to generate 3DCNN probability maps. Despite the presence of a tumor, the 3DCNN was able to map LAN and MOT in regions associated with those networks. Further, the maps were able to follow the structural alterations caused by the GBMs, which can be seen by comparing the lesional/contralesional probability maps for the individual patients. This is especially apparent in the motor network (GBM 1, 2, and 4), which unlike LAN, is highly symmetric across hemispheres. In Figure 5, the slices are selected at the level of the tumor, and in Figure 6 the slices are centered at anatomically similar levels to facilitate comparison across patients. Lastly, in regions especially close to the tumor “core”, the probabilities begin to decline, which is likely due to the presence of necrotic tissue and neurovascular uncoupling distorting the BOLD signal. This can easily be seen in GBM1. Figure 7 shows the probability maps of the MOT network on GBM1 with varying threshold intensities. The figure demonstrates that the MOT probability around the tumor is decreased as compared to the contralateral side. As the threshold changes the asymmetry between the normal side and the area surrounding the tumor becomes more pronounced.

4. Discussion

There is strong evidence in the literature that accurate preoperative functional MRI planning prior to the resection of brain tumors reduces postsurgical morbidity[38]. With current task-based methods, however, the time it takes to get adequate information can extend scan time up to an hour. Thus, there is a high degree of significance to the neurosurgeon in obtaining optimal imaging quality while reducing imaging time and cost. This research was performed primarily in a large number of normal subjects (with only a few examples of application in brain tumor patients) and this was necessitated by the needs of machine learning algorithms. Still, the current work demonstrates the utility of a 3DCNN for voxelwise mapping of language and motor RSNs using only 2.5 minutes of RS-fMRI data (Figures 1–3). This represents a roughly 60% decrease in the quantity of data conventionally thought necessary to map resting state networks[15,39]. Since head motion increases with scan length, a short scan time tends to improve data quality. The problem of head motion is magnified in children, the elderly, and patients uncomfortable in the scanner owing to their disease. Further, in the clinical setting there is a limited amount of time for BOLD fMRI as several anatomic sequences must be obtained in addition to functional imaging. Reducing the imaging time, while maintaining the functional mapping quality, provides a solution to patients requiring a complete radiologic evaluation. Thus, utilization of the 3DCNN could yield more positive imaging outcomes and increased comfort to the patient while preserving accuracy and reducing costs.

The 3DCNN was highly accurate at the voxel level and capable of mapping regions known to associate with LAN and MOT networks (Figures 1 and 2). Further, the varying

topography of the probability maps produced by the 3DCNN show that the model was able to capture individual anatomical variability in patients with brain tumors (Figures 5 and 6). Thus, the 3DCNN does not simply reproduce group level or atlas-based results. This is of vital importance for pre-surgical planning, which requires precise subject-specific mapping to facilitate functional preservation. Lastly, a clinically useful tool should be capable of accurate mapping regardless of the patient demographics and institution utilizing the tool. The 3DCNN achieved 96% validation accuracy on data from multiple studies, originating from multiple sites with different scanners and sequence parameters, representing a broad span of adult ages. These results suggest that the 3DCNN should be widely applicable for purposes of pre-surgical functional mapping.

Tumors induce mass effects, i.e., structural displacements that can distort functional maps[40,41]. Figures 5 and 6 show that the 3DCNN mapping results obtained in 5 patients with glioblastoma multiforme are remarkably similar to the results obtained in healthy individuals, regardless of tumor location. Additionally, we observed inter-hemispheric asymmetries in functional maps, i.e., impaired functional connectivity in the side of the tumor. Tumors destroy functional tissue and induce abnormal neovasculature which can lead to dysfunctional autoregulation and neurovascular uncoupling[42]. The BOLD signal is thought to indirectly reflect neural activity via neurovascular coupling between blood flow, blood volume, and oxygen metabolism[43]. Note the decrease in RSN probability near to the tumor core in the MOT map of patient GBM1. Similar findings could provide a means of assessing regions with the most severe damage (e.g., necrotic tissue) or the greatest abnormality in neurovascular coupling. In contrast, edematous tissue further from the tumor core showed little to no abnormality in the RSN maps. Thus, the maps produced by the 3DCNN can provide significant information that could aid in the management of patients with brain tumors.

For patients with brain tumors, the current standard of care includes a pre-operative T-fMRI study prior to surgery to inform surgical planning. A recent meta-analysis has demonstrated that presurgical planning with T-fMRI improves morbidity and mortality[38]. Multiple studies have demonstrated that RS-fMRI mapping can complement T-fMRI and provide necessary mapping when a patient is unable to cooperate with the study or the task fails for some other reason[10]. The low failure rate of RS-fMRI, automated localization capability of the 3DCNN, and the need for far less scanner time makes the proposed method an attractive choice for pre-operative assessment in tumor patients. Moreover, the current results suggest that there is little difference in the network topographies produced from deep learning-based probability maps derived from RS-fMRI as compared to T-fMRI (Figure 4). Although the obtained maps are topographically comparable, RS-fMRI has several advantages over T-fMRI from the clinical perspective. First, each network mapped with T-fMRI requires a dedicated imaging sequence and patient compliance with the task. Recommendations for T-fMRI paradigm selection emphasize the need for at least 2 task paradigms to fully localize different components of the language system[44]. Thus, at a minimum, for motor and language, 3 T-fMRI runs would need to be performed, which would be approximately an order of magnitude longer in acquisition time. Additionally, RS-fMRI maps may be functionally more specific as compared to T-fMRI. The performance of a task necessarily recruits non-specific brain regions for the performance of the task (see Luckett *et al.*[45] for

discussion). As an example, performing a task requires attention and visual processing to monitor and respond to a cue. These additional functional regions would not be part of the areas mapped using RS-fMRI. This distinction becomes evident when comparing the total area of each network across the brain. The MOT task maps generated from the Neurosynth platform covered 26.2% of the total area of the gray matter, while the 3DCNN maps only covered 12.5%. For LAN mapping, Neurosynth covered 12.9% of the total gray matter area and the 3DCNN 9.3%. Concurrent responses to finger tapping in dorsolateral prefrontal cortex reflect motor planning. Concurrent responses to the language paradigm occur in antero-lateral prefrontal cortex, superior parietal lobule, and non-dominant anterior insula. As previously discussed, these responses reflect cognitive process, e.g., task control, that are not specific to language[10,45]. Other possible reasons for the difference in mappings could be due to the difference in analysis techniques (e.g., our use of an optimized deep learning model versus the aggregation of published maps based on keywords used by Neurosynth), as well as the thresholds used by the different methods.

One limitation of our study is that we did not compare our fMRI results with the gold standard of DCES. Although several studies have taken this approach, by their nature these studies are much smaller in size and thus the data may not be amenable to machine learning tools that require large data sets. Thus, within the scope of this study it was not practical to use DCES data. A follow-up limitation of our study is that unlike in our results in normal subjects, we have no good estimation of mapping accuracy in patients with brain tumors, especially with large tumors that are close to the motor and language networks, which is when the findings are most critical to the surgeon. However, the same limitations and effects of neurovascular uncoupling apply also to T-fMRI in this population. Validation results obtained in both healthy controls (MSC) and patients with brain tumors were limited to a few examples in this study. Future work will involve further model validation on healthy controls collected at multiple institutions to test the effect of varying the amount of data. Similarly, future work will also include a larger tumor patient sample and data acquired using both T-fMRI and RS-fMRI for comparison.

4.1 Conclusion

The current study demonstrates the utility of deep learning for providing accurate mapping of eloquent cortex while using a reduced amount of RS-fMRI data. This result demonstrates an additional advantage of using RS-fMRI for pre-surgical planning beyond the inherent advantages of RS-fMRI, such as not requiring patient compliance with task paradigms. The capability of the 3DCNN to generate accurate functional maps given a minimal amount of data supports functional preservation in patients with brain tumors while increasing imaging efficiency and decreasing cost.

Supplementary Material

Refer to Web version on PubMed Central for supplementary material.

References

1. Vieira S, Pinaya WHL, Mechelli A. Using deep learning to investigate the neuroimaging correlates of psychiatric and neurological disorders: Methods and applications. Neurosci Biobehav Rev. Published online 2017. doi:10.1016/j.neubiorev.2017.01.002
2. Gulati S, Jakola AS, Nerland US, Weber C, Solheim O. The risk of getting worse: surgically acquired deficits, perioperative complications, and functional outcomes after primary resection of glioblastoma. World Neurosurg. 2011;76(6):572–579. [PubMed: 22251506]
3. Lacroix M, Abi-Said D, Fourney DR, et al. A multivariate analysis of 416 patients with glioblastoma multiforme: prognosis, extent of resection, and survival. J Neurosurg. 2001;95(2):190–198.
4. Jakola AS, Unsgård G, Solheim O. Quality of life in patients with intracranial gliomas: the impact of modern image-guided surgery. J Neurosurg. 2011;114(6):1622–1630. [PubMed: 21314270]
5. Hacker CD, Roland JL, Kim AH, Shimony JS, Leuthardt EC. Resting-state network mapping in neurosurgical practice: A review. Neurosurg Focus. Published online 2019. doi:10.3171/2019.9.FOCUS19656
6. Fox MD, Qian T, Madsen JR, et al. Combining task-evoked and spontaneous activity to improve pre-operative brain mapping with fMRI. Neuroimage. 2016;124:714–723. [PubMed: 26408860]
7. Sair HI, Agarwal S, Pillai JJ. Application of resting state functional MR imaging to presurgical mapping: Language mapping. Neuroimaging Clin 2017;27(4):635–644.
8. Silva MA, See AP, Essayed WI, Golby AJ, Tie Y. Challenges and techniques for presurgical brain mapping with functional MRI. NeuroImage Clin. 2018;17:794–803. [PubMed: 29270359]
9. Rosazza C, Zacà D, Bruzzone MG. Pre-surgical brain mapping: to rest or not to rest? Front Neurol. 2018;9:520. [PubMed: 30018589]
10. Park KY, Lee JJ, Dierker D, et al. Mapping language function with task-based vs. resting-state functional MRI. PLoS One. 2020;15(7):e0236423. [PubMed: 32735611]
11. Raichle ME. The restless brain: how intrinsic activity organizes brain function. Philos Trans R Soc B Biol Sci. 2015;370(1668):20140172.
12. Smith SM, Fox PT, Miller KL, et al. Correspondence of the brain's functional architecture during activation and rest. Proc Natl Acad Sci. 2009;106(31):13040–13045. [PubMed: 19620724]
13. Power JD, Schlaggar BL, Petersen SE. Studying brain organization via spontaneous fMRI signal. Neuron. 2014;84(4):681–696. [PubMed: 25459408]
14. Leuthardt EC, Guzman G, Bandt SK, et al. Integration of resting state functional MRI into clinical practice-A large single institution experience. PLoS One. 2018;13(6):e0198349. [PubMed: 29933375]
15. Laumann TO, Gordon EM, Adeyemo B, et al. Functional system and areal organization of a highly sampled individual human brain. Neuron. 2015;87(3):657–670. [PubMed: 26212711]
16. Dosenbach NUF, Koller JM, Earl EA, et al. Real-time motion analytics during brain MRI improve data quality and reduce costs. Neuroimage. 2017;161:80–93. [PubMed: 28803940]
17. Laumann TO, Snyder AZ, Mitra A, et al. On the stability of BOLD fMRI correlations. Cereb cortex. 2017;27(10):4719–4732. [PubMed: 27591147]
18. Gu J, Wang Z, Kuen J, et al. Recent advances in convolutional neural networks. Pattern Recognit. 2018;77:354–377.
19. Bhandari A, Koppen J, Agzarian M. Convolutional neural networks for brain tumour segmentation. Insights Imaging. 2020;11(1):1–9. [PubMed: 31901171]
20. Bernal J, Kushibar K, Asfaw DS, et al. Deep convolutional neural networks for brain image analysis on magnetic resonance imaging: a review. Artif Intell Med. 2019;95:64–81. [PubMed: 30195984]
21. Rudie JD, Gleason T, Barkovich MJ, et al. Clinical assessment of deep learning–based super-resolution for 3D volumetric brain MRI. Radiol Artif Intell. 2022;4(2).
22. Wen D, Wei Z, Zhou Y, Li G, Zhang X, Han W. Deep learning methods to process fmri data and their application in the diagnosis of cognitive impairment: a brief overview and our opinion. Front Neuroinform. 2018;12:23. [PubMed: 29755334]

23. Yin W, Li L, Wu FX. Deep learning for brain disorder diagnosis based on fMRI images. Neurocomputing. 2022;469:332–345.
24. Gordon EM, Laumann TO, Gilmore AW, et al. Precision functional mapping of individual human brains. Neuron. 2017;95(4):791–807. [PubMed: 28757305]
25. Yarkoni T, Poldrack RA, Nichols TE, Van Essen DC, Wager TD. Large-scale automated synthesis of human functional neuroimaging data. Nat Methods. 2011;8(8):665–670. [PubMed: 21706013]
26. Dierker D, Roland JL, Kamran M, et al. Resting-state functional magnetic resonance imaging in presurgical functional mapping: sensorimotor localization. Neuroimaging Clin. 2017;27(4):621–633.
27. Buckner RL, Roffman JL, Smoller JW. Brain Genomics Superstruct Project (GSP). Harvard Dataverse. doi:10.7910/DVN/25833
28. LaMontagne PJ, Benzinger TLS, Morris JC, et al. OASIS-3: longitudinal neuroimaging, clinical, and cognitive dataset for normal aging and Alzheimer disease. MedRxiv. Published online 2019.
29. Power JD, Mitra A, Laumann TO, Snyder AZ, Schlaggar BL, Petersen SE. Methods to detect, characterize, and remove motion artifact in resting state fMRI. Neuroimage. Published online 2014. doi:10.1016/j.neuroimage.2013.08.048
30. Snyder AZ, Nishino T, Shimony J, et al. Covariance and Correlation Analysis of Resting State Functional Magnetic Resonance Imaging Data Acquired in a Clinical Trial of Mindfulness-Based Stress Reduction and Exercise in Older Individuals. Front Neurosci. Published online 2022:335.
31. Hacker CD, Laumann TO, Szrama NP, et al. Resting state network estimation in individual subjects. Neuroimage. Published online 2013. doi:10.1016/j.neuroimage.2013.05.108
32. Park KY, Shimony JS, Chakrabarty S, et al. Optimal Atlas Registration and Resting State Functional Architecture in Patients with Glioblastoma. Published online 2022.
33. Fischl B FreeSurfer. Neuroimage. 2012;62(2):774–781. [PubMed: 22248573]
34. Fox MD, Zhang D, Snyder AZ, Raichle ME. The global signal and observed anticorrelated resting state brain networks. J Neurophysiol. 2009;101(6):3270–3283. [PubMed: 19339462]
35. Smyser CD, Inder TE, Shimony JS, et al. Longitudinal analysis of neural network development in preterm infants. Cereb Cortex. Published online 2010. doi:10.1093/cercor/bhq035
36. Huang G, Liu Z, Van Der Maaten L, Weinberger KQ. Densely connected convolutional networks. In: Proceedings - 30th IEEE Conference on Computer Vision and Pattern Recognition, CVPR 2017. ; 2017. doi:10.1109/CVPR.2017.243
37. Luckett PH, Lee JJ, Park KY, et al. Resting state network mapping in individuals using deep learning. Front Neurol. 2022;13.
38. Luna LP, Sherbaf FG, Sair HI, Mukherjee D, Oliveira IB, Köhler CA. Can preoperative mapping with functional MRI reduce morbidity in brain tumor resection? A systematic review and meta-analysis of 68 observational studies. Radiology. Published online 2021.
39. Van Dijk KRA, Hedden T, Venkataraman A, Evans KC, Lazar SW, Buckner RL. Intrinsic functional connectivity as a tool for human connectomics: Theory, properties, and optimization. J Neurophysiol. Published online 2010. doi:10.1152/jn.00783.2009
40. Holodny AI, Schulder M, Liu WC, Maldjian JA, Kalnin AJ. Decreased BOLD functional MR activation of the motor and sensory cortices adjacent to a glioblastoma multiforme: implications for image-guided neurosurgery. Am J Neuroradiol. 1999;20(4):609–612. [PubMed: 10319970]
41. Fraga de Abreu VH, Peck KK, Petrovich-Brennan NM, Woo KM, Holodny AI. Brain tumors: the influence of tumor type and routine MR imaging characteristics at BOLD functional MR imaging in the primary motor gyrus. Radiology. 2016;281(3):876–883. [PubMed: 27383533]
42. Pronin IN, Holodny AI, Kornienko VN, Petraikin AV, Golovanov AV, Lee HJ. The use of hyperventilation in contrast-enhanced MR of brain tumors. Am J Neuroradiol. 1997;18(9):1705–1708. [PubMed: 9367318]
43. D'Esposito M, Deouell LY, Gazzaley A. Alterations in the BOLD fMRI signal with ageing and disease: a challenge for neuroimaging. Nat Rev Neurosci. 2003;4(11):863–872. [PubMed: 14595398]
44. Black DF, Vachha B, Mian A, et al. American society of functional neuroradiology–recommended fMRI paradigm algorithms for presurgical language assessment. Am J Neuroradiol. 2017;38(10):E65–E73. [PubMed: 28860215]

45. Luckett P, Lee JJ, Park KY, et al. Mapping of the Language Network With Deep Learning. Front Neurol. 2020;11(August):1–12. doi:10.3389/fneur.2020.00819 [PubMed: 32116995]

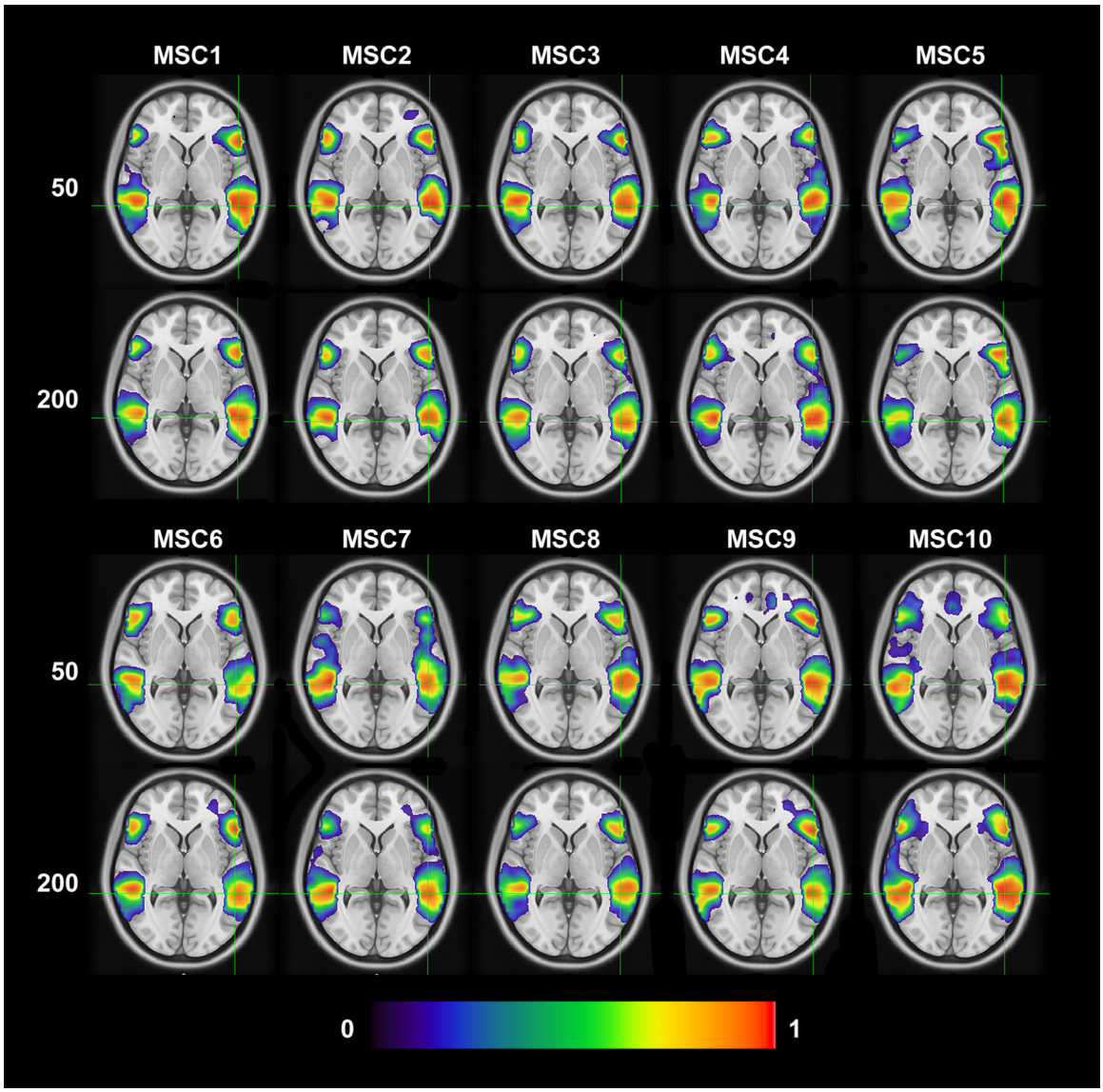

Figure 1:
Comparison of 3DCNN mapping of the language network on MSC subjects using 50 versus 200 time points, corresponding to 2.5 and 10 minutes of data. Top 2 rows correspond to MSC 1–5, bottom 2 rows correspond to MSC 6–10. All images used .1 threshold (slice 71 in MNI atlas).

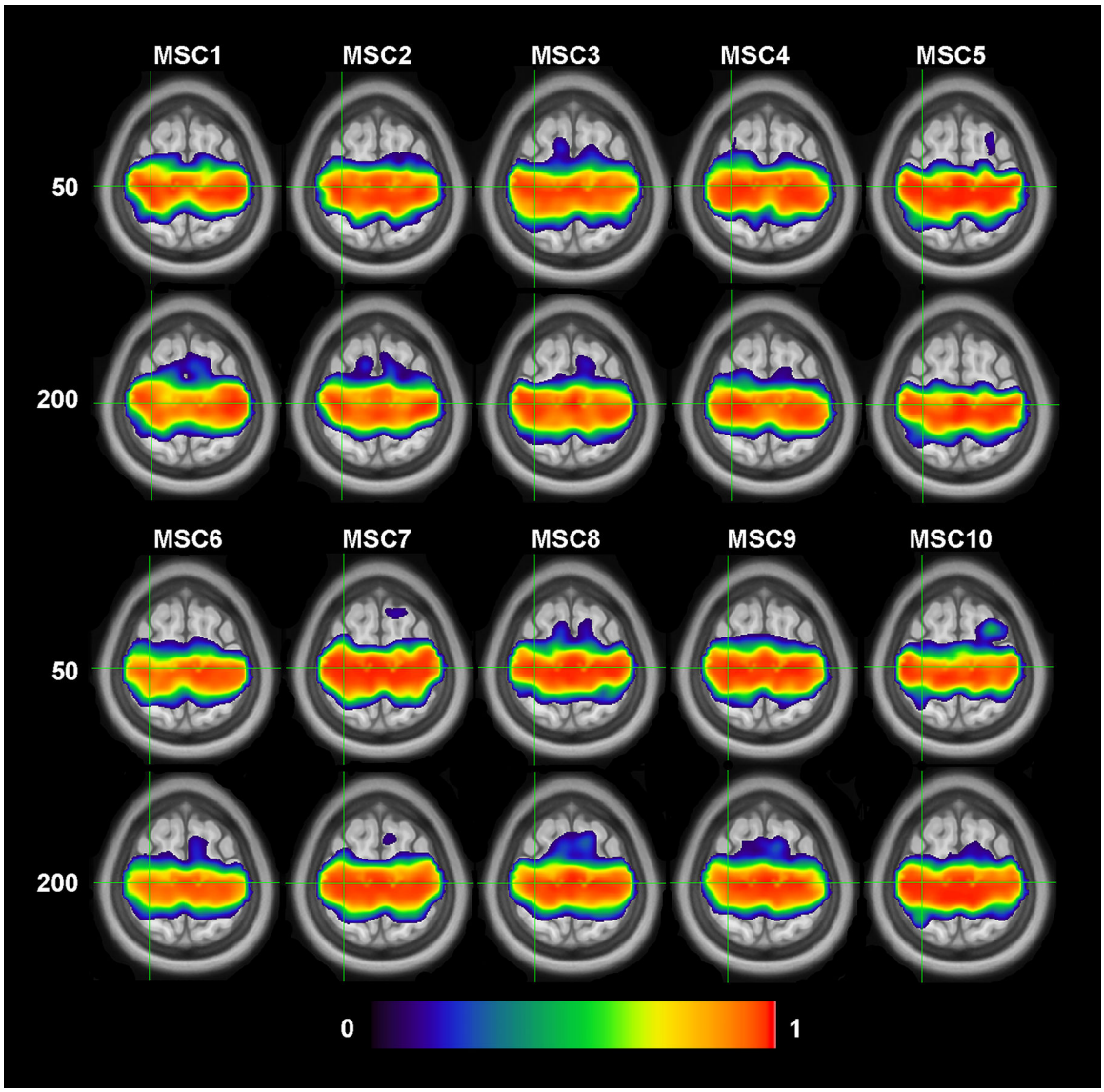

Figure 2:
Comparison of 3DCNN mapping of the motor network on MSC subjects using 50 versus 200 time points, corresponding to 2.5 and 10 minutes of data. Top 2 rows correspond to MSC 1–5 (50 and 200), bottom 2 rows correspond to MSC 6–10. All images used .1 threshold (slice 133 in MNI atlas).

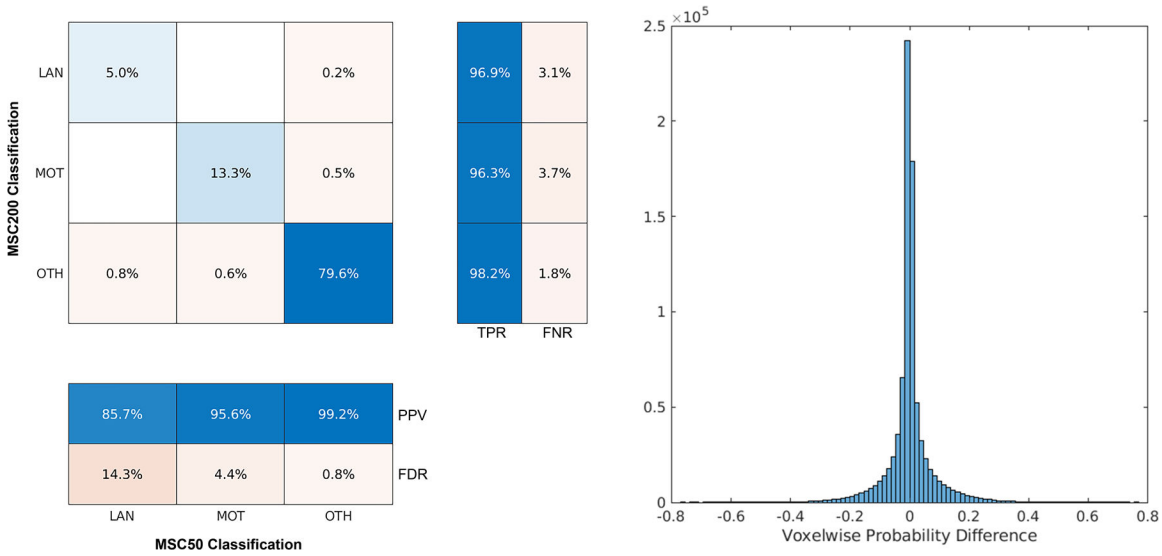

Figure 3:

Left) Voxelwise comparison (winner take all) of MSC data using 50 time points (MSC50) corresponding to approximately 2.5 minutes of data versus 200 time points (MSC200) corresponding to approximately 10 minutes of data. Diagonal elements correspond to the percentage of correctly classified voxels relative to the total number of voxels for the given network. The sum of the diagonal (97.9%) corresponds to the overall accuracy. Right) Histogram of differences when subtracting MSC50 from MSC200. The majority of differences ranged between -.1 and .1.

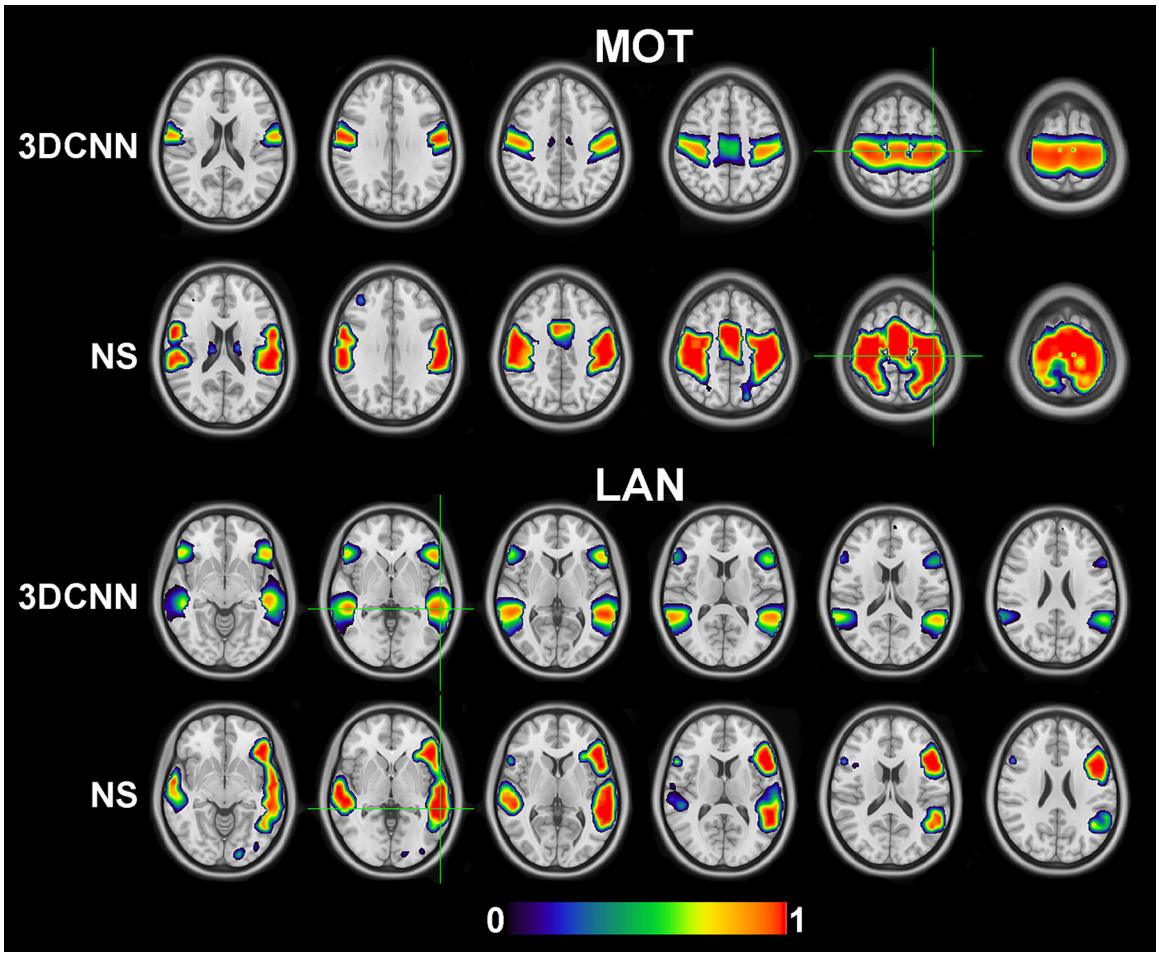

Figure 4:

Comparison of the 3DCNN probability maps averaged over the MSC data with T-fMRI maps generated from the Neurosynth (NS) platform. When calculating the 3DCNN probability maps, only 50 time points (2.5 minutes) were used. A high degree of similarity was observed for both networks, with an MSSI of 0.83 for LAN and 0.80 for MOT.

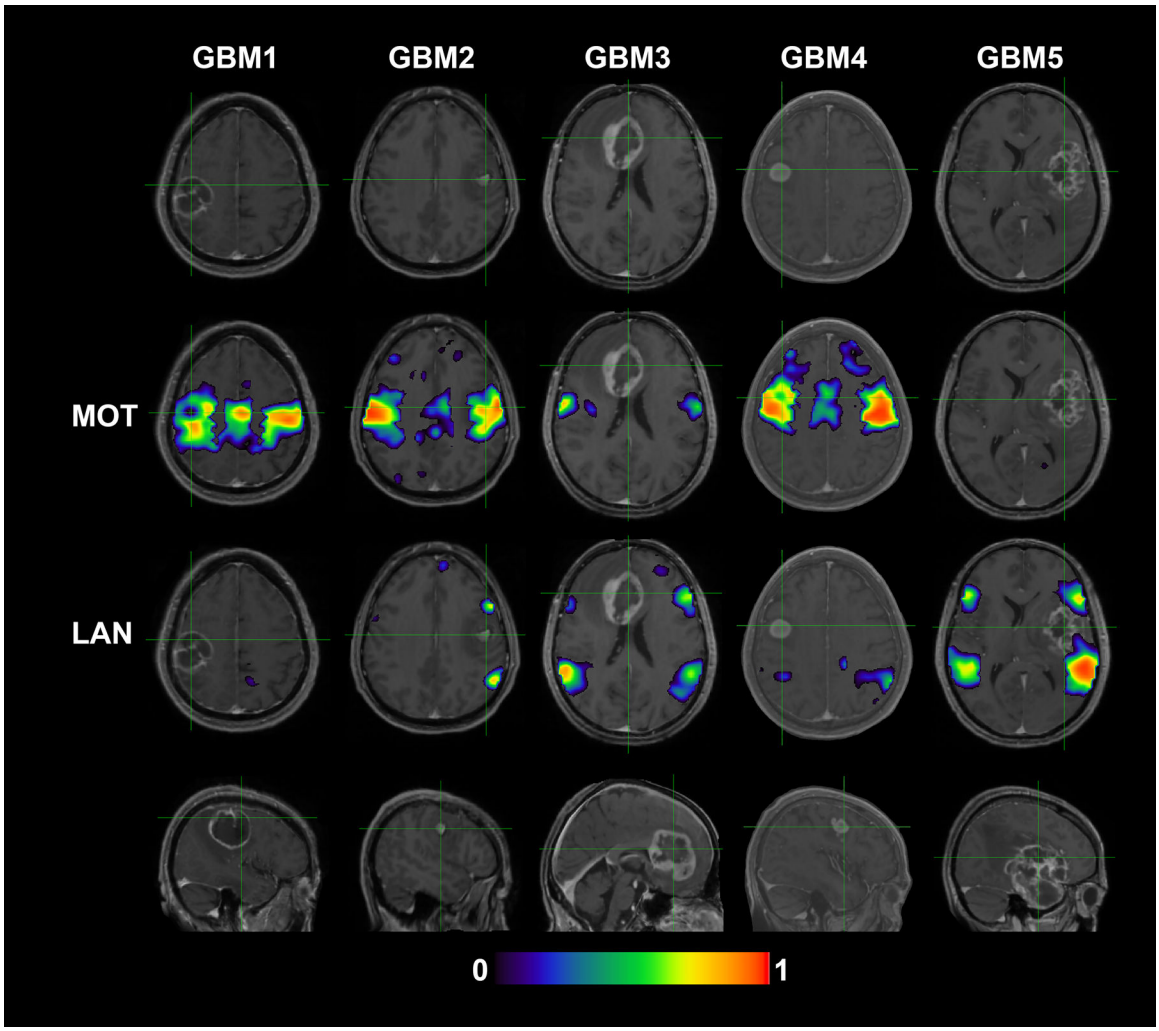

Figure 5:

3DCNN mapping of language and motor networks using 50 time points (2.5 minutes) in GBM patients. Top and bottom row show T1-weighted post contrast axial and sagittal structural views of the tumor. Green cross hairs are centered on the tumor core. Second row shows mappings for the motor network in the given slice (absence of mapping (GBM5) indicates no part of that region encompassed the motor network). Third row shows mappings for the language network. Despite the presence of a tumor, the 3DCNN was able to map LAN and MOT in regions associated with those networks.

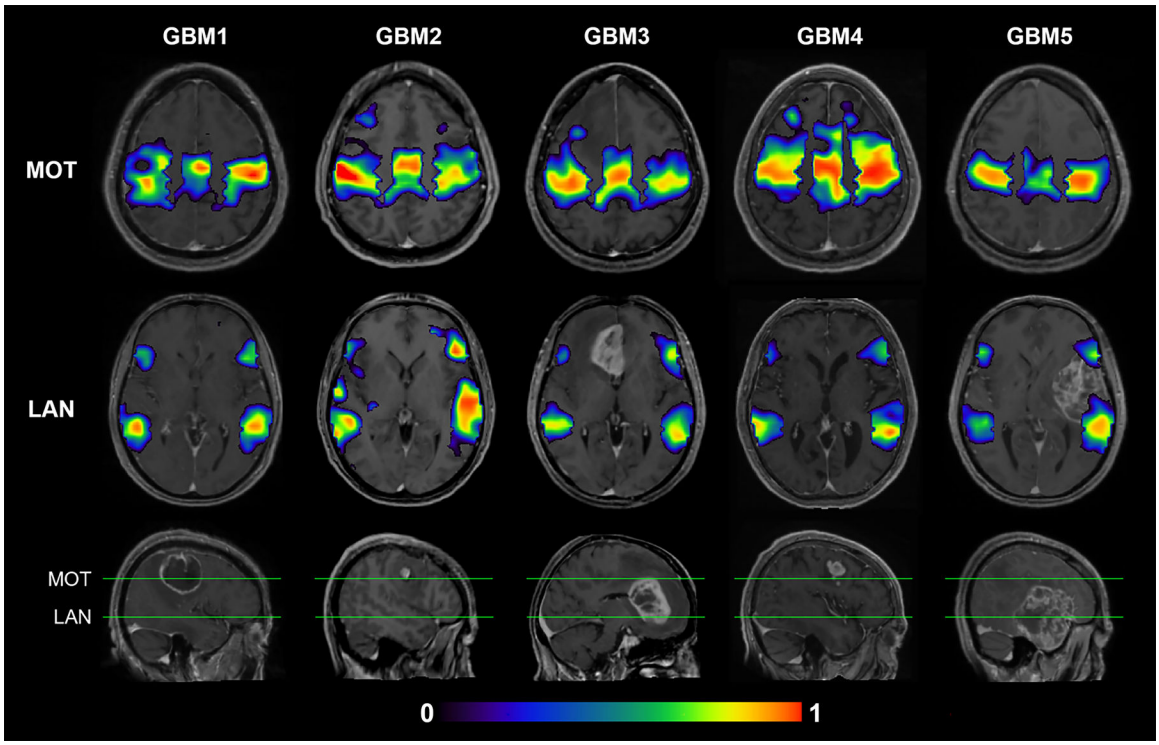

Figure 6:
3DCNN mapping of language and motor networks using 50 time points (2.5 minutes) in GBM patients. First and Second rows show mapping of the motor and language networks on anatomically similar slices of T1-weighted post contrast images. Bottom row shows sagittal structural views of the tumor. Green lines indicate the slice level used in the top two rows. Despite the presence of a tumor, the 3DCNN was able to map LAN and MOT in regions associated with those networks.

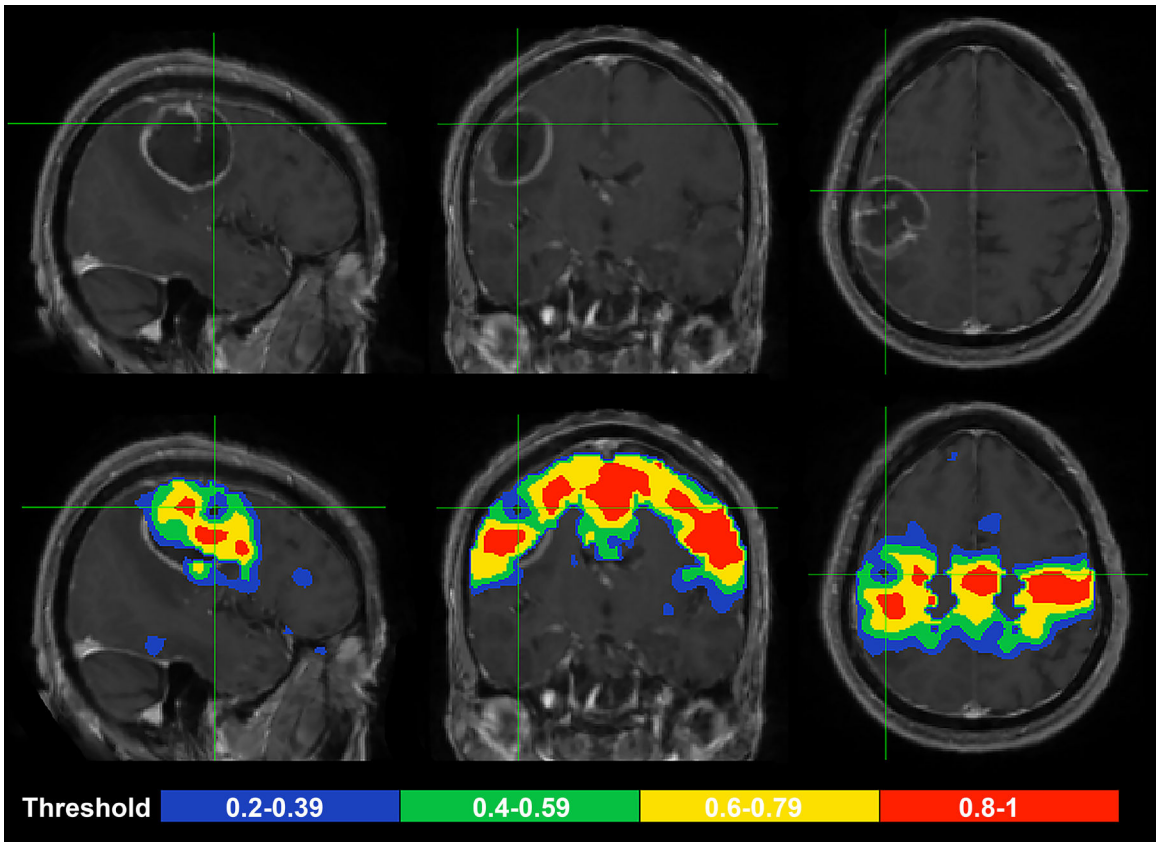

Figure 7:

3DCNN probability maps on GBM1 with varying threshold intensities for the motor network. Probabilities around the tumor are decreased as compared to the contralateral side. As the threshold increases, the region surrounding the tumor falls below the higher threshold value.

Table 1:

Characteristics of training data.

	Total	MEDEX	OASIS3	GSP	HIV
Number of participants	2252	242	665	1139	206
Mean and STD of age	46.6±23.1	70.9±4.7	67.6±7.8	21.3±2.7	37.9±17.1
% Female	60%	71%	60%	59%	52%
Mean and STD for education	15.1±2.4	16.2±2.3	15.9±2.6	14.3±1.9	13.9±2.1
% Caucasian	71%	79%	86%	65%	44%
Scanner		Siemens/ GE	Siemens	Siemens	Trio/Prisma
TR (ms)		2740–2960	2200	3000	2200
Voxel Size (mm^3)		4	4	3	4

TR=repetition time, STD=standard deviation, ms=milliseconds, mm=milimeters